

Spin Filtering and Magneto-Resistive Effect at the Graphene/*h*-BN Ribbon Interface

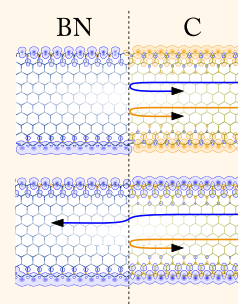
Simon Mutien-Marie Dubois,^{†,*} Xavier Declerck,^{‡,§} J.-C. Charlier,^{‡,§} and Michael C. Payne[†]

[†]Cavendish Laboratory, Theory of Condensed Matter Group, University of Cambridge, JJ Thomson Avenue, Cambridge CB3 0HE, United Kingdom,

[‡]Institute of Condensed Matter and Nanosciences, Nanoscopic Physics, Université Catholique de Louvain, Chemin des étoiles 8, 1348 Louvain-la-Neuve, Belgium, and

[§]European Theoretical Spectroscopy Facility, Belgium

ABSTRACT Advances in the realization of hybrid graphene/*h*-BN materials open new ways to control the electronic properties of graphene nanostructures. In this paper, the structural, electronic, and transport properties of heterojunctions made of bare zigzag-shaped *h*-BN and graphene ribbons are investigated using first-principles techniques. Our results highlight the potential of graphene/*h*-BN junctions for applications in spintronic devices. At first, density functional theory is used to detail the role played by the edge states and dangling bonds in the electronic and magnetic behavior of *h*-BN and graphene ribbons. Then, the electronic conductance of the junction is computed in the framework of Green's function-based scattering theory. In its high-spin configuration, the junction reveals a full spin polarization of the propagating carriers around the Fermi energy, and the magnitude of the transmission probability is predicted to be strongly dependent on the relative orientation of magnetic momenta in the leads.



KEYWORDS: graphene · boron nitride · nanoribbon · spintronic · spin filter · magneto-resistance

Owing to its unique structural and electronic properties, graphene has stirred up enormous attention in science and technology.^{1–6} It is the strongest material known, revealing a Youngs modulus of 1 TPa.⁷ Its ultrahigh room-temperature carrier mobility and large ambipolar response to electric fields make it an ideal platform for applications in electronics.^{3,4,8} Its weak spin–orbit and hyperfine couplings and high predicted spin correlation lengths could be key ingredients for the development of spintronics.^{9–13} More fundamentally, the isolation of graphene has demonstrated that atomically thin crystals can be synthesized in a free-standing form.^{3,8} Indeed, a variety of two-dimensional systems, including single layers of hexagonal boron nitride (*h*-BN), dichalcogenides, and complex oxide planar structures, have been successfully synthesized over the past few years.^{8,14–18} While being an isomorph of graphene with a lattice mismatch of only 1.7%, two-dimensional *h*-BN is a wide gap insulator like its bulk counterpart.^{16,19–21} Recent advances in the synthesis of junctions between electrically conductive graphene and insulating *h*-BN offer new routes to

enhance and tune the electronic, optoelectronic, spintronic, and thermoelectric properties of low-dimensional systems.^{1,2,22–26}

The two-dimensional planar structure and its corresponding quasi-unidimensional forms called *nanoribbons*, where charge carriers are confined in two dimensions and free to move along the ribbon axis, have fascinated the scientific community. Nanoscopic ribbons with varying widths can be realized by various chemical routes,^{27,28} by unzipping nanotubes,²⁹ by lithographic patterning of nanoflakes,^{30,31} or by chemical vapor deposition.³² As demonstrated by theoretical models and experimental characterization, the chemical and topological nature of the edge crucially impacts the chemical, electronic, and magnetic behavior of two-dimensional nanostructures.^{33–37} Indeed, there are two high-symmetry crystallographic directions in two-dimensional honeycomb materials, *armchair* and *zigzag*. Armchair-shaped graphene nanoribbons (*aGNRs*) exhibit full spin degeneracy and an energy gap between the valence and conduction bands that arises from both quantum confinement and edge effects. Zigzag-shaped graphene nanoribbons

* Address correspondence to smmdub@gmail.com.

Received for review March 15, 2013 and accepted May 1, 2013.

Published online May 01, 2013
10.1021/nn401322t

© 2013 American Chemical Society

(zGNRs) exhibit ferromagnetically ordered states at the edges and are predicted to be either metallic or semiconducting depending on the ferro- or anti-ferromagnetic coupling between the edges.^{33,36,38,39} In contrast, all *h*-BN ribbons are reported to be spin-degenerated insulators except for the bare zigzag-shaped ribbons (zBNNRs). The latter are reported to exhibit spin-polarized states at the edge and are predicted to be half-metallic.^{40–42} Note that, depending on the details of the theoretical model used for the prediction, zBNNRs may also exhibit small energy gaps between the spin-polarized conduction and valence bands.⁴¹ Eventually, the energy gap of BN and graphene ribbons can be significantly reduced by a transverse electric field, independently of the topology of the edges.^{39,41,43,44}

Over the years, several approaches have been proposed to control the spin transport in graphene nanostructures. Some proposals are based on defects and impurities engineering. Others rely on the local control of the spin polarization and/or electrostatic potential.^{11,39,45–47} In this paper, we report on the ballistic transmission of charge carriers across the interface between zigzag *h*-BN and graphene ribbons. On the basis of first-principles calculations, our results demonstrate the spin transport characteristics of these junctions. At first, the electronic structures of bare zigzag graphene and *h*-BN ribbons are reviewed. Owing to the presence of spin-polarized edge states and dangling bonds close to the Fermi energy, various magnetic configurations are reported to be accessible at room temperature. In agreement with previous studies, the spin arrangements with the highest total magnetic momenta are found to exhibit a metallic behavior. Then, we focus on the interface between two semi-infinite *h*-BN and graphene zigzag ribbons. The computed electronic structures reveal localized electronic states at the interface as well as a transfer of charge across the heterojunction. Eventually, the low-energy electronic conductances are computed within the Landauer-based Green's function formalism pointing out the interest of these systems for the realization of magnetically switchable nanodevices. Owing to the half-metallic nature of the lead, the low-energy propagating states originating from the *h*-BN ribbon are fully spin-polarized. The transmission probability of the carriers largely depends on the relative spin orientations of the leads. In the parallel configuration, the computed conductance is about $0.8 e^2/h$ in the parallel spin configuration and drops to $0.3 e^2/h$ upon inversion of the magnetic momentum of graphene.

RESULTS AND DISCUSSION

Periodically infinite zigzag graphene and *h*-BN ribbons of 20 Å width without passivation of the edge are first considered. While unpassivated edges are not

expected to be stable at ambient conditions, current studies suggest their stability under inert atmosphere.^{40,48} Various experimental procedures have been derived to eliminate functional groups from the edges, including heat treatment^{49,50} and Joule heating.^{51,52} The relaxed atomic geometries are illustrated in Figure 1. The computed lattice constants are 2.49 and 2.46 Å along *h*-BN and graphene ribbons, respectively. In the presence of bare zigzag-shaped edges, graphene and *h*-BN ribbons exhibit low-energy eigenstates with a peculiar edge structure (*i.e.*, edge states) as well as eigenstates originating from the presence of unsaturated atoms (*i.e.*, dangling bonds). The typical probability densities associated with the edge states and dangling bonds are illustrated in Figure 1f,g. The computed band structures reported in Figure 1a–e emphasize the crucial impact of these particular states on the electronic structure of low-energy carriers. Upon inclusion of the spin degree of freedom within the calculations, graphene and *h*-BN ribbons favor a magnetic ground-state configuration. In order to investigate the different spin configurations, double unit cells (*i.e.*, with two boron atoms at one edge and two nitrogen atoms at the opposite edge in the case of zBNNRs) have been considered. The computed relative energies and total magnetic momenta associated with all of the possible spin configurations are reported in Table 1. In agreement with former predictions,^{41,42} our calculations suggest that carbon and nitrogen edges undergo a significant stabilization upon ferromagnetic order, while anti-ferromagnetic order is metastable (≈ 200 meV/Å higher in energy). On the contrary, ferro- and anti-ferromagnetic orders have very similar energies along the boron edge. The spatial distributions of the most stable spin arrangements are illustrated in Figure 1. In this study, the small spin-orbit coupling in *h*-BN and graphene has been neglected. Two collinear spin channels are considered. The spin states labeled (\uparrow) and (\downarrow) are depicted in blue and orange, respectively.

The energies associated with the most stable configurations are all comprised within 7 meV/Å. Consequently, no prediction of a specific ground state is allowed, and all of these spin configurations are predicted to be accessible at room temperature. Nonetheless, the configurations of highest magnetic momenta (*i.e.*, zBNNR_{↑↑,↑↑} and zGNR_{↑↑,↑↑}) are of particular interest for practical applications as these can be stabilized over the other spin arrangements by an external magnetic field. The band structure depicted in Figure 1b illustrates the half-metallic character of zBNNR_{↑↑,↑↑}. Its half-metallicity originates from the extra stabilization of the edge states along the nitrogen edge. On the contrary, zGNR_{↑↑,↑↑} displays symmetric edges, and edge states from both spin channels are reported at the Fermi energy (see Figure 1e). As will be shown below, the actual symmetry of these edge

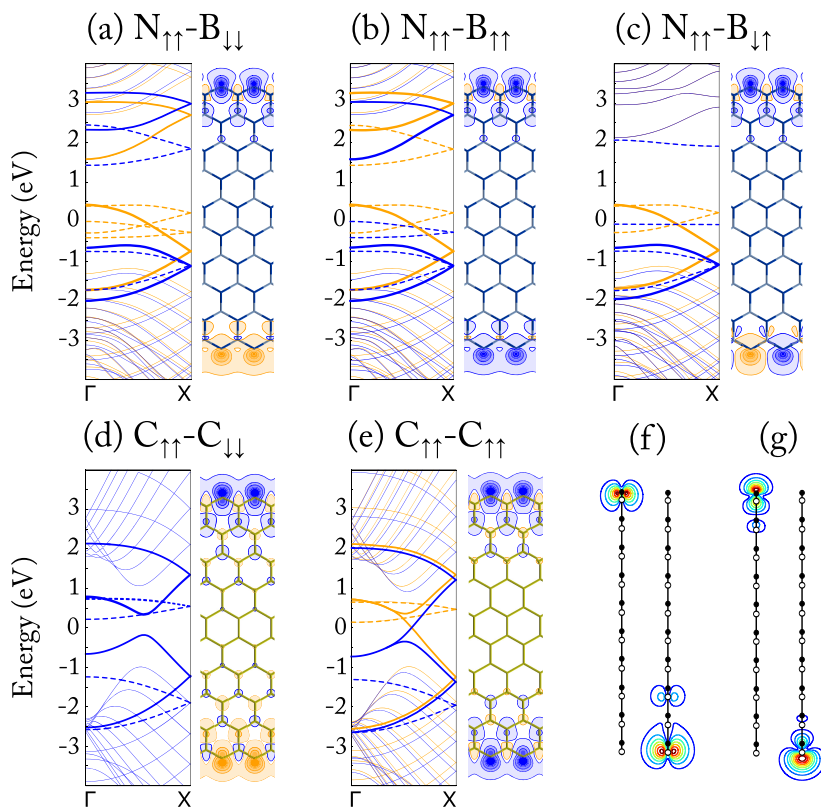


Figure 1. Electronic bands structures, optimized atomic geometries, and spatial representation of the spin density ($\rho_i - \rho_j$) corresponding to the most stable magnetic configurations of 20 Å wide *h*-BN (a–c) and graphene (d,e) zigzag ribbons. Blue and orange lines correspond, respectively, to majority and minority spin channels. In the band structures, plain bold lines correspond to edge states, while dotted bold lines are associated with dangling bonds. The spin densities are integrated over the normal direction to the ribbon plane. The lowest contour lines of $\pm 4 \times 10^{-3} a_0^{-2}$ (a_0 = Bohr radius) are drawn as plain blue and orange lines. Spatial distribution of the eigenstates associated with edge states (f) and dangling bonds (g) of 20 Å wide zBNNR. The modulus of the eigenstate at wave-vector X has been integrated over the ribbon width. The contour lines are equally spaced between the minimum and maximum values of the probability density.

TABLE 1. Relative Energies and Total Magnetic Momenta for Various Spin Configurations of zBNNR and zGNR^a

zBNNR	meV	μ_B	zGNR	meV	μ_B
N _{↑↑} -B _{↑↑}	0	1.87	C _{↑↑} -C _{↓↓}	0	0.00
N _{↑↑} -B _{↓↓}	1	0.00	C _{↑↑} -C _{↑↑}	14	2.55
N _{↑↑} -B _{↑↓}	6	0.94	C _{↑↑} -C _{↓↑}	208	1.27
N _{↑↓} -B _{↑↑}	98	0.94	C _{↑↓} -C _{↑↑}	401	0.00
N _{↑↓} -B _{↓↑}	103	0.00	C _{↑↓} -C _{↓↑}	403	0.00
N _{↑↓} -B _{↑↓}	103	0.00			

^a Relative energies are computed with respect to the ground state. Energies and magnetic momenta are given for *single* unit cells.

states rules the transport properties of the zBNNR/zGNR interface.

In order to investigate the heterostructure made of two semi-infinite graphene and *h*-BN ribbons without passivation at the edge, the geometry of the interface has to be derived first. For that purpose, 30 Å long supercells containing the *h*-BN/graphene interface have been fully optimized with periodic boundary conditions (PBCs) (see Figure 2a). The small lattice mismatch between *h*-BN and graphene creates a local strain at the interface which is progressively screened in the left- and right-hand side ribbons; 7.5 Å away from

the junction, the strain is found to be negligible and the ribbon widths as well as lattice parameters get back to values within 0.1% from equilibrium. The computed atomic positions have then been used in order to build the transport setup illustrated in Figure 2b. The system is partitioned into a central part associated with the interface and two leads made of pristine zBNNR and zGNR. Open boundary conditions (OBCs) are imposed on the system by means of self-energy operators mimicking the coupling of the leads to semi-infinite *h*-BN and graphene ribbons on the left- and right-hand side, respectively. In all calculations, the initial guesses for the electronic degrees of freedom are derived from a standard DFT calculation with PBCs. The OBCs' problem is then solved by computing the retarded Green's function for the system and updating self-consistently the Hamiltonian and charge density.⁵³

As expected from the magnetic behavior of the periodic infinite ribbons, the zigzag-shaped *h*-BN/graphene ribbon (zBN/GNR) presents a multitude of metastable magnetic configurations. Only the configurations with highest magnetic momenta in the leads are considered here. The corresponding spin arrangements, denoted hereafter zBN/GNR_{↑↑} and zBN/GNR_{↑↓},

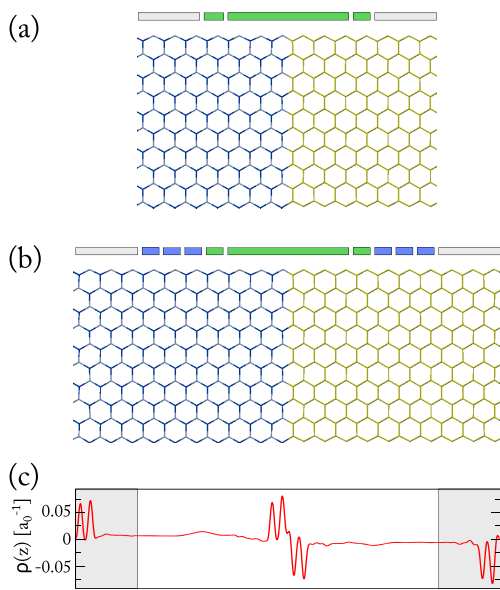


Figure 2. Schematic representation of the supercells used to model the open boundary conditions: (a) zBNNR[1 \times 1 \times 7]/zGNR[1 \times 1 \times 7]; (b) zBNNR[1 \times 1 \times 10]/zGNR[1 \times 1 \times 10]. Colored boxes are used to illustrate the partitioning of the supercells into buffers (in gray), leads (in blue), and interface (in green). (c) Variation of the electronic density along the zBNNR[1 \times 1 \times 10]/zGNR[1 \times 1 \times 10] supercell. The electronic density has been integrated over the plane perpendicular to the ribbon axis and is represented in units of a_0^{-1} (a_0 = Bohr radius).

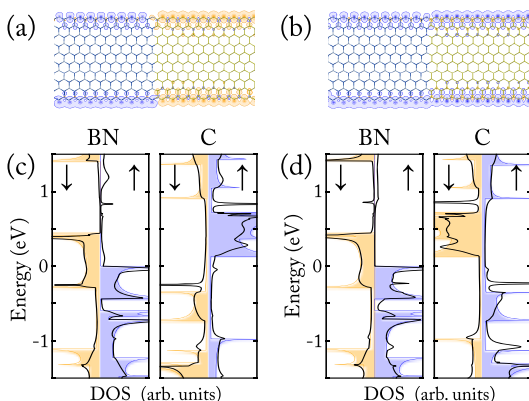


Figure 3. Optimized atomic geometry, spatial representation of the spin density ($\rho_1 - \rho_2$), and density of states corresponding to the junction in the zBN/GNR_t (a,c) and zBN/GNR_t (b,d) configurations. (a,b) Spin density has been integrated over the normal direction to the ribbon plane. Blue and orange contour lines correspond to majority and minority spin channels, respectively. The lowest contour lines drawn are $\pm 4 \times 10^{-3} a_0^{-2}$ (a_0 = Bohr radius). (c,d) Black curves correspond to the DOS of the system projected onto the four zBNNR and zGNR unit cells next to the interface; blue and orange filled curves correspond to the DOS of the semi-infinite periodic zBNNR lead.

are depicted in Figure 3a,b. Independently of the spin distribution, our calculations report a charge transfer from graphene to *h*-BN (see Figure 2c), thus creating a longitudinal dipole at the interface which adds to the transversal dipole of the zBNNR lead. The latter is intrinsic to zBNNR and originates from the polar

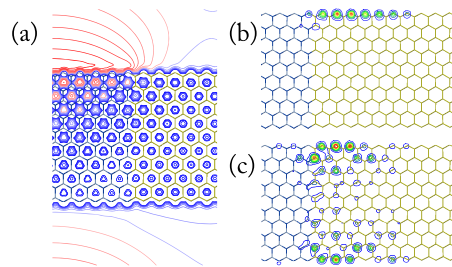


Figure 4. (a) Contour line representation of the electrostatic potential in the vicinity of the zBN/GNR interface. The potential has been averaged over the direction normal to the ribbon plane. Blue and red lines represent, respectively, negative and positive values of the potential. The lowest contours correspond to ± 0.01 Ry, and the spacing is ± 0.01 Ry. (b,c) Spatial representation of the LDOS associated with the sharp peaks located at 855 meV above and 231 meV below the Fermi level in the DOS of zBN/GNR_t. The LDOS has been integrated over the direction normal to the ribbon plane. The lowest contour line corresponds to the value of $0.5 a_0^{-2} E_{Ry}^{-1}$ (a_0 = Bohr radius, E_{Ry} = Rydberg energy).

character of the boron–nitrogen bond. The computed electrostatic potential across the junction is reported in Figure 4a. The density of states (DOS) projected onto the interface region illustrates the local energy distribution of electronic states (see Figure 3c,d). As a consequence of the electrostatic perturbation at the interface, localized electronic states are reported, mainly located on the graphene side of the junction. The local densities of states (LDOS) associated with the narrow peaks in the DOS at 231 meV below and 855 meV above the Fermi level are depicted in Figure 4b,c. Localized within the first few zGNR unit cells, these states present a mirror symmetry with respect to the ribbon plane. Their spatial distribution is reminiscent of the zGNR edge states associated with the Van Hove singularities at 351 meV below and 722 meV above the Fermi level.

The OBCs imposed in the simulations naturally allow one to describe the scattering of carriers from one lead to the other across the *h*-BN/graphene interface. The computed retarded Green's function of the system contains all of the information about the electronic structure of the interface in equilibrium with the semi-infinite leads. Within the approximation of coherent propagation of carriers, the zero-bias conductance can be directly extracted by means of the Fisher-Lee relation.^{54,55}

The transmission probabilities corresponding to the zBN/GNR_t and zBN/GNR_t junctions in the absence of external bias voltage are reported in Figure 5a,b. In the semi-infinite leads, the low-energy solution to the scattering problem are the Bloch states associated with the edge states and the dangling bonds. As there is an energy mismatch between the zBNNR and zGNR dangling bonds, these Bloch states cannot be transmitted coherently across the interface. Therefore, at low energies, the propagating scattering states

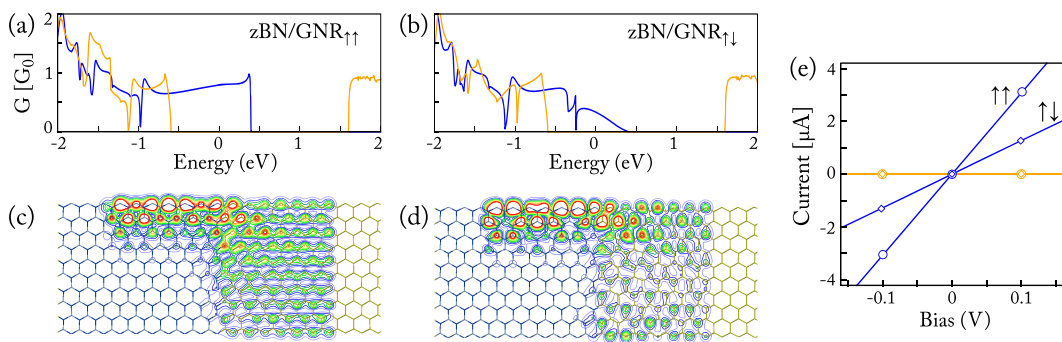


Figure 5. Zero-bias quantum conductance for the junction in the $z\text{BN}/\text{GNR}_{\uparrow\uparrow}$ (a) and $z\text{BN}/\text{GNR}_{\uparrow\downarrow}$ (b) configurations. Blue and orange lines correspond, respectively, to majority and minority spin channels. Spatial representation of the left incoming transmission eigenchannel at Fermi energy across the junction in the $z\text{BN}/\text{GNR}_{\uparrow\uparrow}$ (c) and $z\text{BN}/\text{GNR}_{\uparrow\downarrow}$ (d) configurations. The transmission eigenchannel has been integrated over the direction normal to the ribbon plane. The lowest contour line corresponds to a value of $0.05 a_0^{-2} E_{\text{Ry}}^{-1}$ (a_0 = Bohr radius, E_{Ry} = Rydberg energy). (e) Spin-resolved I/V curves for the junction in the $z\text{BN}/\text{GNR}_{\uparrow\uparrow}$ (circles) and $z\text{BN}/\text{GNR}_{\uparrow\downarrow}$ (diamonds). The lines are computed directly from the equilibrium transmission probabilities depicted in (a) and (b), while the circles and diamonds are derived from fully out-of-equilibrium calculations.

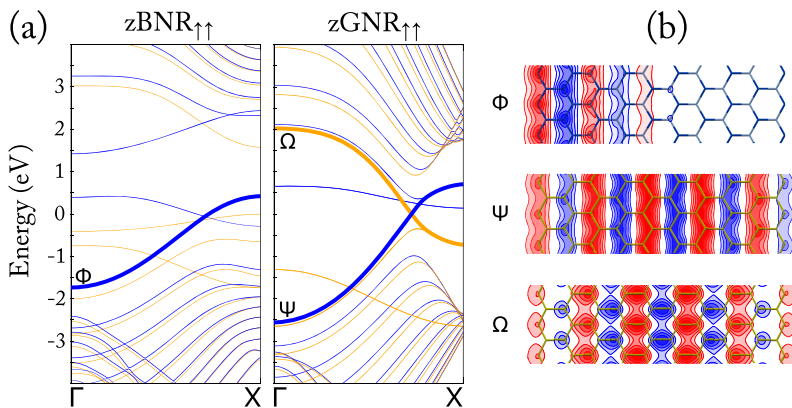


Figure 6. (a) Electronic band structure of pristine zBNNR and zGNR ribbons in the high-spin configurations. Blue and orange lines correspond, respectively, to the minority and majority spin channels. For clarity, the band structures illustrated here correspond to single unit cells (i.e., no bands folding). The bold lines are associated with the Bloch states accounting for the low-energy quantum conductance of the zBN/GNR junction. (b) Spatial representation of the Bloch states playing a particular role in the transport properties of the junction. The zBNNR edge state localized on the nitrogen side of the ribbon is labeled Φ . The zGNR bonding and antibonding edge states are labeled Ψ and Ω , respectively. The real part of the eigenstates has been integrated over the direction normal to the ribbon plane. Blue and red lines correspond to positive and negative values. Twelve contour lines are equally spaced between the lowest and highest values of the eigenstates.

contributing to the conductance only originate from the zBNNR and zGNR edge states. This situation is illustrated in Figure 6a, where the bands available for low-energy scattering are highlighted. Because of the half-metallic character of the zBNNR lead, the left incoming and outgoing components of the propagating states belong to the zBNNR minority spin channel regardless of the spin configuration of the zGNR lead. It accounts for the full spin polarization of the transmission function around the Fermi energy and emphasizes the potential of such junctions for ballistic spin filtering devices.

The low-energy zBNNR incoming states correspond to bonding zBNNR edge states localized on the nitrogen edge. In the $z\text{BN}/\text{GNR}_{\uparrow\uparrow}$ configuration, zBNNR incoming states are scattered into the bonding zGNR edge states. As illustrated in Figure 6b, those Bloch states present a similar symmetry and give rise to high transmission probability. On the contrary, in the

$z\text{BN}/\text{GNR}_{\uparrow\downarrow}$ configuration, zBNNR incoming states are scattered into the antibonding zGNR edge states. In this configuration, the incoming and scattered Bloch states are nearly orthogonal and the transmission probability is strongly reduced. When switching from the $z\text{BN}/\text{GNR}_{\uparrow\uparrow}$ to the $z\text{BN}/\text{GNR}_{\uparrow\downarrow}$ configuration, the equilibrium conductance changes from 0.8 to 0.3 e^2/h . The impact of the magnetic configuration on the equilibrium conductance is further illustrated in Figure 5c,d. The computed left incoming transmission eigenchannels allows visualization of the scattering of the zBNNR incoming state into the bonding (Figure 5c) and antibonding zGNR edge states (Figure 5d). In agreement with the computed conductances, the transmitted probability density significantly decreases with the switching of the junction from its $z\text{BN}/\text{GNR}_{\uparrow\uparrow}$ to its $z\text{BN}/\text{GNR}_{\uparrow\downarrow}$ configuration. In the presence of a finite bias between the leads, the spin filtering and magneto-resistive characteristics of the zBN/GNR interface give rise to a

fully spin-polarized current whose intensity depends on the spin configuration of the leads (see Figure 5e). One notes that the values of the current computed in the out-of-equilibrium situations at biases of -0.1 and 0.1 V are in close agreement with the I/V curves derived from the symmetric integration of the equilibrium transmission probabilities.

CONCLUSIONS

The electronic structure of *h*-BN and graphene ribbons with bare zigzag edges has been reviewed by means of first-principles calculations. In particular, the crucial role played by the dangling bonds and the edge states on both the electronic and transport properties of low-energy carriers is detailed. In agreement with previous works, our calculations highlight the half-metallic and metallic character of these structures in their high-spin configurations. The structural and electronic properties of zBN/GNR interfaces have then been investigated. By coupling equilibrium DFT calculations with the self-consistent Green's function formalism, the *open* nature of the system has been fully taken into account. The computed electronic density

reveals the creation of a longitudinal electric dipole at the interface as well as the formation of localized states at the termination of the graphene ribbon. Because of their localized character, these states do not affect the transport properties of the system. Eventually, the conductance of the zBN/GNR junction has been computed for two experimentally relevant magnetic configurations, revealing the potential of those systems for spintronic applications. Owing to the half-metallic character of bare zigzag *h*-BN ribbons and the good coupling zBNNR and zGNR edge states at the interface, zBN/GNR junctions act as passive spin filters. If realized in practice, these junctions would enable a perfect filtering of the spin transport simply by applying a magnetic field sufficiently strong so as to favor the high-spin configuration of the *h*-BN and graphene ribbons. Attaching both ends of the junction to ferromagnetic electrodes would allow control of both the electrostatic potential across the junction and the spin configuration of the leads. As the magnitude of the low-energy transmission probabilities is directly controlled by the magnetic orientation of the leads, such setup could be used to modulate the amplitude of the spin current.

METHODS

Ground-state calculations on *h*-BN and graphene ribbons were performed using the density functional theory^{56,57} within the local spin density approximation. The interaction between valence electrons and ionic cores has been modeled using norm-conserving pseudopotentials.⁵⁸ Numerical atomic orbital basis sets (double- ζ plus polarization) were used to expand the wave functions, as implemented in the SIESTA code.⁵⁹ Real-space quantities were represented on a grid characterized by a cutoff equivalent to 350 Ry. The integration of the first Brillouin zone was achieved by summation over regular grids of k -points. The number of k -points has been chosen so that its product by the unit cell length is about 100 Å. The energy levels were populated using a Fermi–Dirac distribution with an electronic temperature of 300 K. The ionic positions and lattice constants of the pristine nanoribbons as well as of the 30 Å long supercell depicted in Figure 3 were fully optimized so that the Hellmann–Feynman forces acting on individual atoms and on the unit cell were reduced to less than 0.01 and 0.05 eV/Å, respectively. Test calculations were performed on pristine graphene and the *h*-BN atomic sheet; the computed lattice constants were 2.46 and 2.48 Å, respectively. A direct energy gap of 4.6 eV was reported for the *h*-BN atomic sheet, in good agreement with previous first-principles calculations.²⁰ Eventually, the basis set used has been further validated by comparison of the results presented in this paper with zBNNRs and zGNRs electronic structures computed with the ABINIT code.⁶⁰ For this comparison, a cutoff energy of 30 Ha was used to expand the electronic wave functions using a plane-wave basis set. No significant discrepancies were noted.

The geometry of the transport setup has been derived from the relaxed atomic position of a zBNNR[1 × 1 × 7]/zGNR[1 × 1 × 7] supercell (*i.e.*, 30 Å long). More specifically, the relaxed atomic positions of the fourth zBNNR and zGNR unit cells were duplicated four times in order to build the geometry corresponding to the leads. A zBNNR[1 × 1 × 10]/zGNR[1 × 1 × 10] supercell (*i.e.*, 50 Å long and 400 atoms) was used in order to compute the initial guess for the electronic density associated with the transport setup, while the open boundary conditions (OBCs) were imposed on the inner zBNNR[1 × 1 × 7]/zGNR[1 × 1 × 7] supercell

corresponding to the interface. Note that, in this setup, the first three zBNNR unit cells and the last three zGNR unit cells serve as buffer layers in order to allow the efficient solving of Poisson's equation in reciprocal space. OBCs were treated by means of contact self-energy operators derived from the one-particle Hamiltonian computed at the DFT level as implemented in the TRANSIESTA code.⁵³ In order to update self-consistently the Hamiltonian and electronic density of the interface, the retarded Green's function of the system has been integrated in the complex energy plane along a standard contour enclosing six poles of the Fermi–Dirac distribution function and using, respectively, 11 and 40 integration points for the line and circle segments.⁵³ The out-of-equilibrium density matrix has been derived from the Green's function by using 48 integration points along the real energy axis. The LDOS represented in Figure 4b,c have been computed as $\rho(r,E) = (1/\pi)^2 \text{Im}[G(r,r,E) - (G(r,r,E + \Delta E) + G(r,r,E - \Delta E))/2]$ with $\Delta E = 20$ meV. This procedure was required in order to isolate the contribution of the peaks from the contribution of the edge states. The energy-normalized transmission eigen-channels represented in Figure 5c,d have been computed directly from the retarded Green's function as prescribed by Paulsson *et al.*⁶¹

Conflict of Interest: The authors declare no competing financial interest.

Acknowledgment. The authors thank A.R. Botello-Méndez for valuable discussions. S.M.-M.D. and M.C.P. acknowledge funding from EPSRC under Grant EP/G055904/1. J.-C.C. acknowledges financial support from the F.R.S.-FNRS. Parts of this work are directly connected to the ARC “Graphene Stresstronics” sponsored by the Communauté Française de Belgique. Computational resources have been provided by the supercomputing facilities of the Université Catholique de Louvain (CISM).

REFERENCES AND NOTES

1. Ci, L.; Song, L.; Jin, C.; Jariwala, D.; Wu, D.; Li, Y.; Srivastava, A.; Wang, Z. F.; Storr, K.; Balicas, L.; *et al.* Atomic Layers of Hybridized Boron Nitride and Graphene Domains. *Nat. Mater.* **2010**, 9, 430–435.

2. Levendorf, M. P.; Kim, C.-J.; Brown, L.; Huang, P. Y.; Havener, R. W.; Muller, D. A.; Park, J. Graphene and Boron Nitride Lateral Heterostructures for Atomically Thin Circuitry. *Nature* **2012**, *488*, 627–632.
3. Novoselov, K. S.; Geim, A. K.; Morozov, S. V.; Jiang, D.; Zhang, Y.; Dubonos, S. V.; Grigorieva, I. V.; Firsov, A. A. Electric Field Effect in Atomically Thin Carbon Films. *Science* **2004**, *306*, 666–669.
4. Zhang, Y.; Tan, Y.-W.; Stormer, H. L.; Kim, P. Experimental Observation of the Quantum Hall Effect and Berry's Phase in Graphene. *Nature* **2005**, *438*, 201–204.
5. Berger, C.; Song, Z.; Li, X.; Wu, X.; Brown, N.; Naud, C.; Mayou, D.; Li, T.; Hass, J.; Marchenkov, A. N.; et al. Electronic Confinement and Coherence in Patterned Epitaxial Graphene. *Science* **2006**, *312*, 1191–1196.
6. Geim, A. K. Graphene: Status and Prospects. *Science* **2009**, *324*, 1530–1534.
7. Lee, C.; Wei, X.; Kysar, J. W.; Hone, J. Measurement of the Elastic Properties and Intrinsic Strength of Monolayer Graphene. *Science* **2008**, *321*, 385–388.
8. Novoselov, K. S.; Jiang, D.; Schedin, F.; Booth, T. J.; Khotkevich, V. V.; Morozov, S. V.; Geim, A. K. Two-Dimensional Atomic Crystals. *Proc. Natl. Acad. Sci. U.S.A.* **2005**, *102*, 10451–10453.
9. Kane, C. L.; Mele, E. J. Quantum Spin Hall Effect in Graphene. *Phys. Rev. Lett.* **2005**, *95*, 226801.
10. Hill, E.; Geim, A.; Novoselov, K.; Schedin, F.; Blake, P. Graphene Spin Valve Devices. *IEEE Trans. Magn.* **2006**, *42*, 2694–2696.
11. Yazyev, O. V. Emergence of Magnetism in Graphene Materials and Nanostructures. *Rep. Prog. Phys.* **2010**, *73*, 056501.
12. Pesin, D.; MacDonald, A. H. Spintronics and Pseudospintronics in Graphene and Topological Insulators. *Nat. Mater.* **2012**, *11*, 409–416.
13. Slubak, B.; Martin, M.-B.; Deranlot, C.; Servet, B.; Xavier, S.; Mattana, R.; Sprinkle, M.; Berger, C.; De Heer, W. A.; Petroff, F.; et al. Highly Efficient Spin Transport in Epitaxial Graphene on SiC. *Nat. Phys.* **2012**, *8*, 557–561.
14. Seo, J.-w.; Jun, Y.-w.; Park, S.-w.; Nah, H.; Moon, T.; Park, B.; Kim, J.-G.; Kim, Y. J.; Cheon, J. Two-Dimensional Nanosheet Crystals. *Angew. Chem., Int. Ed.* **2007**, *46*, 8828–8831.
15. Ayari, A.; Cobas, E.; Ogundadege, O.; Fuhrer, M. S. Realization and Electrical Characterization of Ultrathin Crystals of Layered Transition-Metal Dichalcogenides. *J. Appl. Phys.* **2007**, *101*, 014507.
16. Pacilé, D.; Meyer, J. C.; Girit, C. O.; Zettl, A. The Two-Dimensional Phase of Boron Nitride: Few-Atomic-Layer Sheets and Suspended Membranes. *Appl. Phys. Lett.* **2008**, *92*, 133107.
17. Oyler, K. D.; Ke, X.; Sines, I. T.; Schiffer, P.; Schaak, R. E. Chemical Synthesis of Two-Dimensional Iron Chalcogenide Nanosheets: FeSe, FeTe, Fe(Se,Te), and FeTe₂. *Chem. Mater.* **2009**, *21*, 3655–3661.
18. Alem, N.; Erni, R.; Kisielowski, C.; Rossell, M. D.; Gannett, W.; Zettl, A. Atomically Thin Hexagonal Boron Nitride Probed by Ultrahigh-Resolution Transmission Electron Microscopy. *Phys. Rev. B* **2009**, *80*, 155425.
19. Nagashima, A.; Tejima, N.; Gamou, Y.; Kawai, T.; Oshima, C. Electronic Structure of Monolayer Hexagonal Boron Nitride Physisorbed on Metal Surfaces. *Phys. Rev. Lett.* **1995**, *75*, 3918–3921.
20. Blase, X.; Rubio, A.; Louie, S. G.; Cohen, M. L. Quasiparticle Band Structure of Bulk Hexagonal Boron Nitride and Related Systems. *Phys. Rev. B* **1995**, *51*, 6868–6875.
21. Watanabe, K.; Taniguchi, T.; Kanda, H. Direct-Bandgap Properties and Evidence for Ultraviolet Lasing of Hexagonal Boron Nitride Single Crystal. *Nat. Mater.* **2004**, *3*, 404–409.
22. Rubio, A. Hybridized Graphene: Nanoscale Patchworks. *Nat. Mater.* **2010**, *9*, 379–380.
23. Liu, Z.; Ma, L.; Shi, G.; Zhou, W.; Gong, Y.; Lei, S.; Yang, X.; Zhang, J.; Yu, J.; Hackenberg, K. P.; et al. In-Plane Heterostructures of Graphene and Hexagonal Boron Nitride with Controlled Domain Sizes. *Nat. Nanotechnol.* **2013**, *8*, 119–124.
24. Blase, X.; Charlier, J. C.; DeVita, A.; Car, R. Theory of Composite BxCyNz Nanotube Heterojunctions. *Appl. Phys. Lett.* **1997**, *70*, 197–199.
25. Yang, K.; Chen, Y.; D'Agosta, R.; Xie, Y.; Zhong, J.; Rubio, A. Enhanced Thermoelectric Properties in Hybrid Graphene/Boron Nitride Nanoribbons. *Phys. Rev. B* **2012**, *86*, 045425.
26. Song, L.; Balicas, L.; Mowbray, D. J.; Capaz, R. B.; Storr, K.; Ci, L.; Jariwala, D.; Kurth, S.; Louie, S. G.; Rubio, A.; et al. Anomalous Insulator-Metal Transition in Boron Nitride-Graphene Hybrid Atomic Layers. *Phys. Rev. B* **2012**, *86*, 075429.
27. Ci, L.; Xu, Z.; Wang, L.; Gao, W.; Ding, F. Controlled Nanocutting of Graphene. *Nano Res.* **2008**, *1*, 116–122.
28. Datta, S. S.; Strachan, D. R.; Khamis, S. M.; Johnson, A. T. C. Crystallographic Etching of Few-Layer Graphene. *Nano Lett.* **2008**, *8*, 1912–1915.
29. Kosynkin, D. V.; Higginbotham, A. L.; Sinitskii, A.; Lomeda, J. R.; Dimiev, A.; Price, B. K.; Tour, J. M. Longitudinal Unzipping of Carbon Nanotubes To Form Graphene Nanoribbons. *Nature* **2009**, *458*, 872–876.
30. Tapaszó, L.; Dobrik, G.; Lambin, P.; Biró, L. P. Tailoring the Atomic Structure of Graphene Nanoribbons by Scanning Tunnelling Microscope Lithography. *Nat. Nanotechnol.* **2008**, *3*, 397–401.
31. Jiao, L.; Zhang, L.; Wang, X.; Diankov, G.; Dai, H. Narrow Graphene Nanoribbons from Carbon Nanotubes. *Nature* **2009**, *458*, 877–880.
32. Campos-Delgado, J.; Romo-Herrera, J. M.; Jia, X.; Cullen, D. A.; Muramatsu, H.; Kim, Y. A.; Hayashi, T.; Ren, Z.; Smith, D. J.; Okuno, Y.; et al. Bulk Production of a New Form of sp² Carbon: Crystalline Graphene Nanoribbons. *Nano Lett.* **2008**, *8*, 2773–2778.
33. Son, Y.-W.; Cohen, M. L.; Louie, S. G. Energy Gaps in Graphene Nanoribbons. *Phys. Rev. Lett.* **2006**, *97*, 216803.
34. Han, M. Y.; Özylmaz, B.; Zhang, Y.; Kim, P. Energy Band-Gap Engineering of Graphene Nanoribbons. *Phys. Rev. Lett.* **2007**, *98*, 206805.
35. Ritter, K. A.; Lyding, J. W. The Influence of Edge Structure on the Electronic Properties of Graphene Quantum Dots and Nanoribbons. *Nat. Mater.* **2009**, *8*, 235–242.
36. Dubois, S. M.-M.; Zanolli, Z.; Declerck, X.; Charlier, J.-C. Electronic Properties and Quantum Transport in Graphene-Based Nanostructures. *Eur. Phys. J. B* **2009**, *72*, 1–24.
37. Dubois, S. M.-M.; Lopez-Bezanilla, A.; Cresti, A.; Triozon, F.; Biel, B.; Charlier, J.-C.; Roche, S. Quantum Transport in Graphene Nanoribbons: Effects of Edge Reconstruction and Chemical Reactivity. *ACS Nano* **2010**, *4*, 1971–1976.
38. Barone, V.; Hod, O.; Scuseria, G. E. Electronic Structure and Stability of Semiconducting Graphene Nanoribbons. *Nano Lett.* **2006**, *6*, 2748–2754.
39. Son, Y.-W.; Cohen, M. L.; Louie, S. G. Half-Metallic Graphene Nanoribbons. *Nature* **2006**, *444*, 347–349.
40. Terrones, M.; Charlier, J.-C.; Gloter, A.; Cruz-Silva, E.; Terrés, E.; Li, Y. B.; Vinu, A.; Zanolli, Z.; Dominguez, J. M.; Terrones, H.; et al. Experimental and Theoretical Studies Suggesting the Possibility of Metallic Boron Nitride Edges in Porous Nanoribbons. *Nano Lett.* **2008**, *8*, 1026–1032.
41. Barone, V.; Peralta, J. E. Magnetic Boron Nitride Nanoribbons with Tunable Electronic Properties. *Nano Lett.* **2008**, *8*, 2210–2214.
42. Topsakal, M.; Aktürk, E.; Ciraci, S. First-Principles Study of Two- and One-Dimensional Honeycomb Structures of Boron Nitride. *Phys. Rev. B* **2009**, *79*, 115442.
43. Park, C.-H.; Louie, S. G. Energy Gaps and Stark Effect in Boron Nitride Nanoribbons. *Nano Lett.* **2008**, *8*, 2200–2203.
44. Zhang, Z.; Guo, W. Energy-Gap Modulation of BN Ribbons by Transverse Electric Fields: First-Principles Calculations. *Phys. Rev. B* **2008**, *77*, 075403.
45. Kim, W. Y.; Kim, S. Prediction of Very Large Values of Magnetoresistance in a Graphene Nanoribbon Device. *Nat. Nanotechnol.* **2008**, *3*, 408–412.
46. Wimmer, M.; Adagideli, I.; Berber, S.; Tomanek, D.; Richter, K. Spin Currents in Rough Graphene Nanoribbons: Universal Fluctuations and Spin Injection. *Phys. Rev. Lett.* **2008**, *100*, 177207.

47. Munoz-Rojas, F.; Fernandez-Rossier, J.; Palacios, J. J. Giant Magnetoresistance in Ultrasmall Graphene Based Devices. *Phys. Rev. Lett.* **2009**, *102*, 136810.

48. Girit, C. O.; Meyer, J. C.; Erni, R.; Rossell, M. D.; Kisielowski, C.; Yang, L.; Park, C.-H.; Crommie, M. F.; Cohen, M. L.; Louie, S. G.; *et al.* Graphene at the Edge: Stability and Dynamics. *Science* **2009**, *323*, 1705–1708.

49. Kobayashi, Y.; Fukui, K.-i.; Enoki, T.; Kusakabe, K.; Kaburagi, Y. Observation of Zigzag and Armchair Edges of Graphite Using Scanning Tunneling Microscopy and Spectroscopy. *Phys. Rev. B* **2005**, *71*, 193406.

50. Kobayashi, Y.; Fukui, K.-i.; Enoki, T.; Kusakabe, K. Edge State on Hydrogen-Terminated Graphite Edges Investigated by Scanning Tunneling Microscopy. *Phys. Rev. B* **2006**, *73*, 125415.

51. Jia, X.; Campos-Delgado, J.; Gracia-Espino, E. E.; Hofmann, M.; Muramatsu, H.; Kim, Y. A.; Hayashi, T.; Endo, M.; Kong, J.; Terrones, M.; *et al.* Loop Formation in Graphitic Nanoribbon Edges Using Furnace Heating or Joule Heating. *J. Vac. Sci. Technol., B* **2009**, *27*, 1996–2002.

52. Jia, X.; Hofmann, M.; Meunier, V.; Sumpter, B. G.; Campos-Delgado, J.; Romo-Herrera, J. M.; Son, H.; Hsieh, Y.-P.; Reina, A.; Kong, J.; *et al.* Controlled Formation of Sharp Zigzag and Armchair Edges in Graphitic Nanoribbons. *Science* **2009**, *323*, 1701–1705.

53. Brandbyge, M.; Mozos, J. L.; Ordejon, P.; Taylor, J.; Stokbro, K. Density-Functional Method for Nonequilibrium Electron Transport. *Phys. Rev. B* **2002**, *65*, 165401.

54. Fisher, D. S.; Lee, P. A. Relation between Conductivity and Transmission Matrix. *Phys. Rev. B* **1981**, *23*, 6851–6854.

55. Meir, Y.; Wingreen, N. S. Landauer Formula for the Current through an Interacting Electron Region. *Phys. Rev. Lett.* **1992**, *68*, 2512–2515.

56. Hohenberg, P.; Kohn, W. Inhomogeneous Electron Gas. *Phys. Rev.* **1964**, *136*, B864–B871.

57. Kohn, W.; Sham, L. J. Self-Consistent Equations Including Exchange and Correlation Effects. *Phys. Rev.* **1965**, *140*, A1133–A1138.

58. Troullier, N.; Martins, J. L. Efficient Pseudopotentials for Plane-Wave Calculations. *Phys. Rev. B* **1991**, *43*, 1993–2006.

59. Soler, J. M.; Artacho, E.; Gale, J. D.; Garcia, A.; Junquera, J.; Ordejon, P.; Sanchez-Portal, D. The SIESTA Method for *Ab Initio* Order-N Materials Simulation. *J. Phys.: Condens. Matter* **2002**, *14*, 2745–2779.

60. Gonze, X.; Beuken, J.-M.; Caracas, R.; Detraux, F.; Fuchs, M.; Rignanese, G.-M.; Sindic, L.; Verstraete, M.; Zerah, G.; Jollet, F.; *et al.* First-Principles Computation of Material Properties: The ABINIT Software Project. *Comput. Mater. Sci.* **2002**, *25*, 478–492.

61. Paulsson, M.; Brandbyge, M. Transmission Eigenchannels from Nonequilibrium Green's Functions. *Phys. Rev. B* **2007**, *76*, 115117.